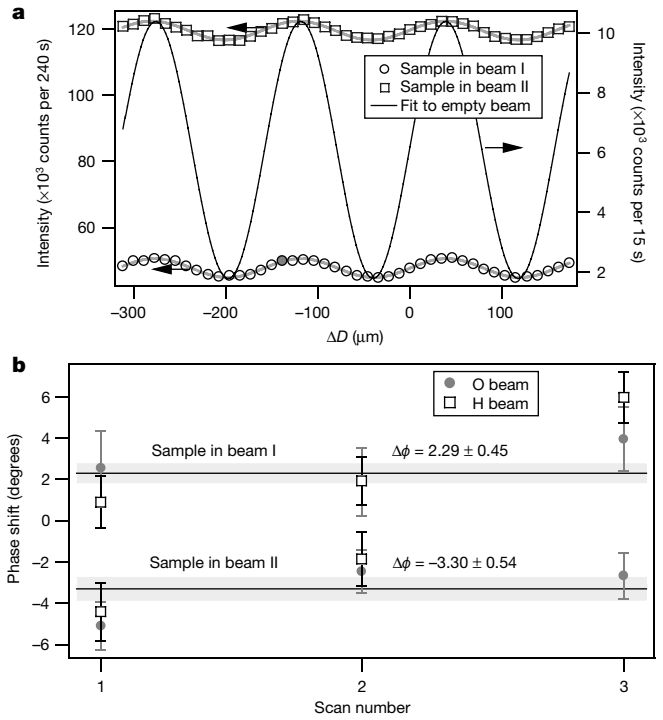

Figure 4 Typical interference pattern with and without the phase-shifting slit system (**a**) and the collection of the results of various scans (**b**). ΔD denotes the path length difference of beam I and II within the phase shifter.

the walls but which do contribute to the expected phase shift; we also find beam components that are totally reflected from the walls or that pass through the walls, neither of which contribute to a measurable contrast owing to smearing effects.

The measurements were performed at the neutron interferometer set-up S18 at the Institut Laue-Langevin in Grenoble. A skew symmetric interferometer has been used and adjusted to a wavelength of $\lambda = 1.89(3)$ Å, which corresponds to an incident energy of $E_{in} = 0.0278(8)$ eV. The slit system has been put into beams I and II, and outside both beams (Fig. 3). This sweep procedure permits the measurement of small phase shifts at low contrast. The slit system consists of 186 slits with a width of 22.1 μm and the same wall thickness and a length of 20 mm. Silicon wafers were used as wall material and spacers. After careful adjustment to the parallel position ($\alpha \cong 0°$) various scans have been made where Fig. 4 shows a typical result and the summary result of all scans. As expected, the opposite phase shift becomes visible for both beams and this is a good indication that spurious phases have been excluded. The measured value of the confinement-induced phase shift is $\Delta\phi = 2.8(4)°$, which is in rather good agreement with the expected value ($\Delta\phi \cong 2.5°$).

The wavefunctions within the slits show an interesting pattern (wavefunction carpets) which could be exploited in more detail in future. When the slits are oriented horizontally, a triangular-shaped potential due to the gravity effect occurs that changes mainly the low-lying levels from $E_0 = 0.417$ peV to $E_{0'} = 0.2904$ peV or from $E_1 = 1.669$ peV to $E_{1'} = 1.702$ peV (refs 15, 16). For such experiments the interferometer would have to be rotated to the horizontal direction as well because the large wave packet extension needed for these experiments exists only in the direction normal to the reflecting crystal planes of the interferometer[17,18]. A different situation occurs when absorbing wall materials are used. Other effects may occur when a time-dependent interaction (for example, vibrating walls) can cause transitions between different energy levels. □

Received 22 January; accepted 17 April 2002; doi:10.1038/nature00773.

1. Lévy-Leblond, J. M. A geometrical quantum phase effect. *Phys. Lett. A* **125,** 441–442 (1987).
2. Greenberger, D. M. A new non-local effect in quantum mechanics. *Physica B* **151,** 374–377 (1988).
3. Rauch, H. & Werner, S. A. *Neutron Interferometry* (Clarendon, Oxford, 2000).
4. Casimir, H. B. G. & Polder, D. Influence of retardation on the London-van der Waals forces. *Phys. Rev.* **73,** 360–372 (1948).
5. Haroche, S. & Raimond, J. M. Cavity quantum electrodynamics. *Sci. Am.* **268,** 26–33 (1993).
6. Fonda, L., Ghirardi, G. C., Rimini, A. & Weber, T. On the quantum foundations of the experimental decay law. *Nuovo Cimento A* **15,** 689–704 (1973).
7. Misra, B. & Sudarshan, E. C. G. The Zeno's paradox in quantum theory. *J. Math. Phys.* **18,** 756–763 (1977).
8. Grisenti, R. E. *et al.* Determination of atom-surface van der Waals potentials from transmission diffraction intensities. *Phys. Rev. Lett.* **83,** 1755–1758 (1999).
9. Hegerfeldt, G. C. & Koehler, T. Deviations from classical optics in matter diffraction and determination of the size of weakly bound molecules. *Phys. Rev. A* **61,** 023606-1–023606-10 (2000).
10. Ferry, D. K., Grubin, H., Jacobini, C. & Jauho, A. J. (eds) *Quantum Transport in Ultrasmall Devices* (Plenum, New York, 1995).
11. Salomon, C., Dalibard, J., Aspect, A., Metcalf, H. & Cohen-Tannoudji, C. Channeling atoms in a laser standing wave. *Phys. Rev. Lett.* **59,** 1659–1662 (1987).
12. Keller, C. *et al.* Adiabatic following in standing-wave diffraction of atoms. *Appl. Phys. B* **69,** 303–309 (1999).
13. Allman, B. E., Cimmino, A., Griffin, S. L. & Klein, A. G. Quantum phase shift caused by spatial confinement. *Found. Phys.* **29,** 325–332 (1999).
14. Nesvizhevsky, V. V. *et al.* Quantum states of neutrons in the Earth's gravitational field. *Nature* **415,** 297–299 (2002).
15. Flügge, S. *Practical Quantum Mechanics* (Springer, Berlin, 1971).
16. Pokotilovski & Yu, N. Quantum phase shift of spatially confined de Broglie waves in a gravitational field. *Phys. Lett. A* **248,** 114–116 (1998).
17. Rauch, H., Wölwitsch, H., Kaiser, H., Clothier, R. & Werner, S. A. Measurement and characterization of the three-dimensional coherence function in neutron interferometry. *Phys. Rev. A* **53,** 902–908 (1996).
18. Rauch, H. & Summhammer, J. Neutron interferometer absorption experiments in the quantum limit. *Phys. Rev. A* **46,** 7284–7287 (1992).

Acknowledgements

This work was supported by the Austrian Science Foundation and a TMR-Network of the European Union EU. Useful discussions with J. Summhammer and D. Petrascheck are gratefully acknowledged.

Competing interests statement

The authors declare that they have no competing financial interests.

Correspondence and requests for materials should be addressed to H.R. (e-mail: rauch@ati.ac.at).

Marine aerosol formation from biogenic iodine emissions

Colin D. O'Dowd*†, Jose L. Jimenez‡, Roya Bahreini‡, Richard C. Flagan‡, John H. Seinfeld‡, Kaarle Hämeri§, Liisa Pirjola†‖, Markku Kulmala† S. Gerard Jennings* & Thorsten Hoffmann¶

** Department of Physics, National University of Ireland, Galway, Ireland*
† Division of Atmospheric Sciences, Department of Physical Sciences, P.O. Box 64, FIN-00014, University of Helsinki, Helsinki, Finland
‡ Departments of Environmental Science and Engineering and Chemical Engineering, California Institute of Technology, 210-41, 1200 E. California Boulevard, Pasadena, USA
§ Finnish Institute for Occupational Health, Topeliuksenkatu 41a, FIN-00250, Helsinki, Finland
‖ Helsinki Polytechnic Technology, PL 4020, FIN-00099, Helsinki, Finland
¶ Institute of Spectrochemistry and Applied Spectroscopy, 44139 Dortmund, Germany

The formation of marine aerosols and cloud condensation nuclei—from which marine clouds originate—depends ultimately on the availability of new, nanometre-scale particles in the marine boundary layer. Because marine aerosols and clouds scatter incoming radiation and contribute a cooling effect to the Earth's radiation budget[1], new particle production is important

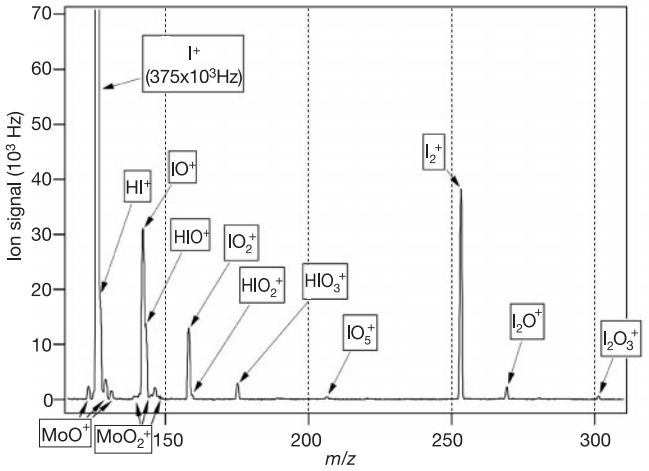

Figure 1 Observed aerosol mass spectrum from chamber experiments as measured by the aerosol mass spectrometer. The aerosol resulted from the photo-oxidation of CH_2I_2 in the presence of O_3 in pure laboratory air. The observed peaks are consistent with particles composed of iodine oxides and/or iodine oxyacids, and possibly also water. The molybdenum oxide peaks observed in the spectrum are probably due to the oxidation of the molybdenum particle vaporizer of the spectrometer by iodine oxyacids contained in the sampled particles.

in climate regulation. It has been suggested that sulphuric acid—derived from the oxidation of dimethyl sulphide—is responsible for the production of marine aerosols and cloud condensation nuclei. It was accordingly proposed that algae producing dimethyl sulphide play a role in climate regulation[2], but this has been difficult to prove and, consequently, the processes controlling marine particle formation remains largely undetermined[3,4]. Here, using smog chamber experiments under coastal atmospheric conditions, we demonstrate that new particles can form from condensable iodine-containing vapours, which are the photolysis products of biogenic iodocarbons emitted from marine algae. Moreover, we illustrate, using aerosol formation models, that concentrations of condensable iodine-containing vapours over the open ocean are sufficient to influence marine particle formation. We suggest therefore that marine iodocarbon emissions have a potentially significant effect on global radiative forcing.

There are two steps required for the production of new particles by gas-to-particle conversion processes (secondary particle formation). First, a critical embryo, or thermodynamically stable cluster of the order of 1 nm in size, must be formed from the coalescence of precursor vapours (homogeneous nucleation)[5]. Second, these stable clusters must grow rapidly enough, by coagulation and/or condensation, to quasi-stable particle sizes of 3–4 nm (particle formation) before they collide by diffusion with larger, pre-existing, particles[6] and are subsequently captured (diffusion decreases as $1/D^2$, where D is the particle diameter). Once new particles reach sizes of a few nanometres, there is a net increase in the particle number concentration.

Recent simulations of ternary H_2SO_4–H_2O–NH_3 nucleation[7] have shown that under typical atmospheric concentrations of H_2SO_4, nucleation of thermodynamically stable clusters can readily occur; however, production of new particles via growth by vapour condensation is unlikely, owing to insufficient supply of H_2SO_4. Although H_2SO_4 could be responsible for the production of thermodynamically stable clusters, other vapours are required for particle production. The most comprehensive studies[8] into marine aerosol nucleation have focused on coastal environments, where regular and intense particle production events are encountered owing to the higher intensity of biological processes in coastal areas. Such particle production is independent of peak H_2SO_4 concentrations[9], suggesting a hitherto unknown marine particle production mechanism. Experimental measurements on new particle composition have ruled out a chemical composition dominated by H_2SO_4 (ref. 10), and identified iodine in these particles[11]. Consequently, the production of particles in the coastal zone by condensable iodine vapours (CIVs) resulting from the photolysis of biogenic CH_2I_2 has been proposed[8].

To test this hypothesis, we conducted experiments (see Methods) in the Caltech smog chamber[12] into the particle production ability of CH_2I_2 undergoing photolysis in the presence of ozone, and we present results confirming that this is a viable mechanism for particle production down to atmospheric concentrations[13]. No particles were formed unless CH_2I_2, O_3 and ultraviolet radiation were simultaneously present in the chamber. When ultraviolet radiation was introduced after CH_2I_2 and O_3 had been mixed throughout the chamber, rapid homogeneous nucleation occurred, followed by condensation and coagulation growth. This behaviour was observed for all experiments for CH_2I_2 levels from 50 parts per billion (50 p.p.b.) down to the lowest CH_2I_2 concentration achievable in this chamber of 0.015 p.p.b. ($\sim 4 \times 10^8$ molecules cm^{-3}).

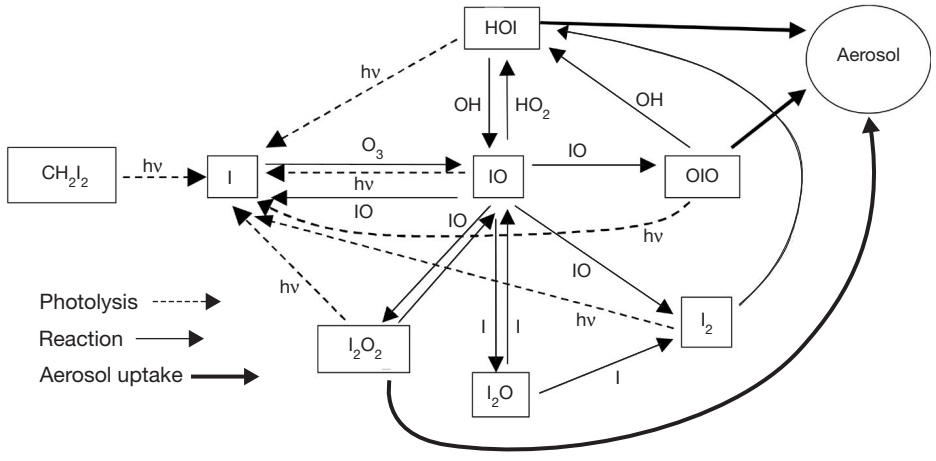

Figure 2 Chemical pathway from CH_2I_2 to aerosol production, on the basis of the current state of knowledge of the gas-phase chemistry. Quantitative rates are given in refs 18 and 30.

Decreasing the CH_2I_2 concentration did not change the nucleation or growth phenomenology, but resulted in longer timescales for both processes.

Particles formed under dry conditions possessed a fractal morphology, whereas particles formed under humid conditions (relative humidity ~65%) were more compact and dense. No other significant differences in the nucleation or growth behaviour as a function of humidity was observed. Reducing the intensity of the ultraviolet radiation slowed the particle formation processes without changing their qualitative features. Analysis of the resultant aerosol chemical composition, using an aerosol mass spectrometer, revealed the following mass/charge (m/z) peaks: OH^+, H_2O^+, I^+, HI^+, IO^+, HIO^+, IO_2^+, HIO_2^+, HIO_3^+, IO_5^+, I_2^+, I_2O^+ and $I_2O_3^+$ (Fig. 1). These peaks are consistent with particles composed of iodine oxides and/or iodine oxyacids, and possibly also water. Particle composition did not change with particle size or with time in the experiment.

The chemical mechanisms associated with the particle production is presented in Fig. 2. There are three possible pathways to form CIVs: (1) CH_2I_2 is rapidly photolysed, releasing an I atom which reacts with O_3 to produce IO. IO in turn reacts with itself to produce OIO, which can nucleate to produce I_2O_4 and higher-order iodine oxide polymers; (2) IO can also self-react to produce I_2O_2, which can participate in aerosol formation; (3) IO can react with HO_2 to produce condensable HOI. At the lowest concentrations of less than 20–200 parts per trillion (p.p.t.) CH_2I_2, HOI is the dominant CIV, whereas iodine oxides dominate at higher concentrations. There results show that nucleation and condensation of CIVs occurs under atmospheric coastal conditions, and that this mechanism must be considered viable in terms of contributing to the marine aerosol population.

Estimates[14–17] of the global flux of iodine from macroalgae are of the order of 10^7–10^8 g I yr^{-1}, but this source is limited to coastal zones. Microalgae (phytoplankton), on the other hand, are found all over the ocean, and are estimated to contribute 10^9–10^{10} g I yr^{-1}. The global ocean source, however, is estimated[14–17] to be 10^{11}–10^{12} g I yr^{-1}, but the main contributor to this source of iodine, in addition to micro and macro algae, is currently unidentified, although there is strong evidence that bacteria can synthesize CH_3I, which could account for the missing source[17]. Nevertheless, taking a global marine source of 10^{12} g I yr^{-1} and a globally averaged marine surface-mixed-layer height of 300 m, the source rate of iodine atoms is estimated at 1.4×10^3 atoms cm^{-3} s^{-1}. This open-ocean source of iodine atoms compares favourably to the recent estimate of 1×10^4 atoms cm^{-3} required to explain the observed concentration of IO and OIO (up to 1.6×10^8 cm^{-3}) over the open ocean[18,19].

We simulate, using a marine aerosol model (see Methods), the production of new particles resulting from condensation of CIVs onto thermodynamically stable cluster embryos. The simulation (Fig. 3) is started just before sunrise, and as dimethylsulphide is photochemically destroyed, H_2SO_4 production also increases, leading to a peak concentration of 2.5×10^6 molecules cm^{-3}. At these typical H_2SO_4 concentrations, the concentration of thermodynamically stable clusters reaches a maximum of ~5,000 cm^{-3}, resulting from a peak nucleation rate of 4 cm^{-3} s^{-1}, but barely-detectable new particle formation results in sizes larger than 3 nm. When an additional CIV source (Q) of 10^3 cm^{-3} s^{-1} is included, slight particle production results after a few hours, resulting from an enhancement in condensable vapours of 0.5×10^6 cm^{-3}. Increasing Q to 5×10^3, 10×10^3 and 25×10^3 molecules cm^{-3} s^{-1} leads to a CIV concentration of respectively 2.5×10^6, 5×10^6 and 12×10^6 molecules cm^{-3}, and increases the particle concentration from 518 cm^{-3} to 555 cm^{-3}, 614 cm^{-3} and 804 cm^{-3}, respectively. Clearly, increasing the source rate of CIVs significantly increases the production rate of new particles.

The initial and final aerosol size distributions are given in Fig. 4 for all simulations. As the CIV vapour concentration increases, the final concentration of the nucleation mode increases, as does the

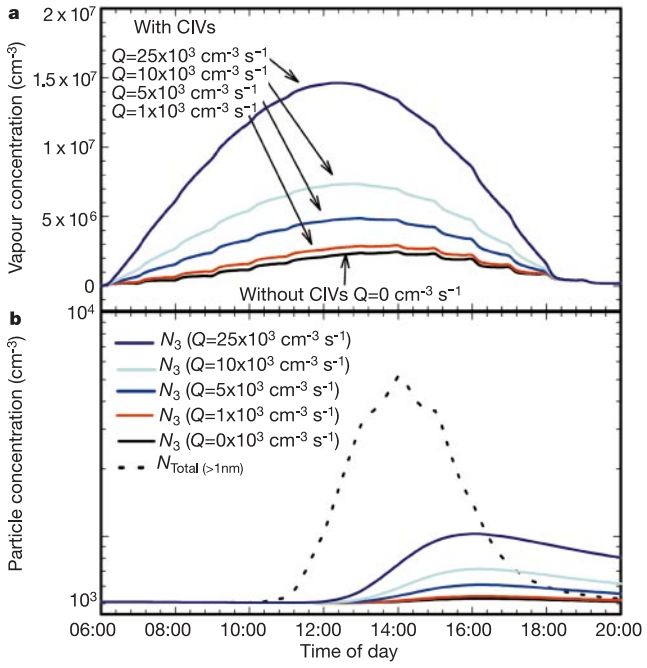

Figure 3 Model simulations of condensable vapour and aerosol concentrations in the marine boundary layer. **a**, Combined concentration of H_2SO_4 and condensable iodine vapours (CIVs) for CIV source rates (Q) of 0, 10^3, 5×10^3, 10×10^3 and 25×10^3 molecules cm^{-3} s^{-1} and a dimethylsulphide concentration of 20 p.p.t. (5.6×10^8 molecules cm^{-3}). Oscillations in the vapour concentration occur owing to the variation in the pre-existing aerosol condensation sink as the aerosol surface area responds to changes in relative humidity during air parcel cycling through the boundary layer. **b**, Predicted particle concentration (cm^{-3}) at sizes larger than 1 nm (N_{total}), including thermodynamically stable clusters; and detectable particle sizes of 3 nm and greater (N_3) for CIV source rates of 0, 10^3, 5×10^3, 10×10^3 and 25×10^3 molecules cm^{-3} s^{-1}.

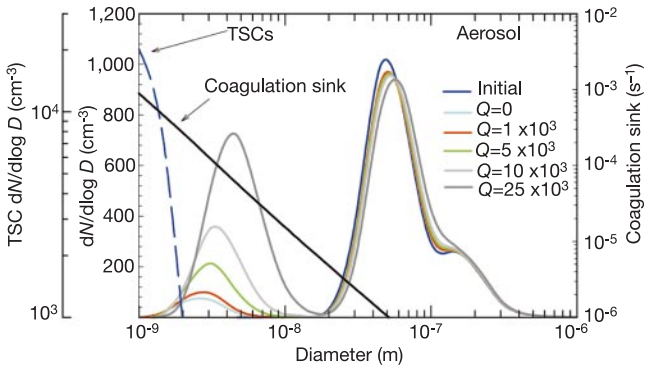

Figure 4 Initial (local time 06:00) and predicted final (local time 20:00) aerosol size distributions for CIV source rates (Q) of 0, 10^3, 5×10^3, 10×10^3 and 25×10^3 molecules cm^{-3} s^{-1}. Also shown (note different scale) is the maximum concentration of thermodynamically stable clusters (TSCs) during the period of peak particle production (local time 14:00). The coagulation sink (the rate of loss of particles per second owing to coagulation with the pre-existing aerosol) as a function of particle size is superimposed on the figure. N, number of particles.

mean modal size (up to 6 nm). At a condensable vapour concentration of 2.4×10^6 cm^{-3} ($Q = 0$), the nucleation mode comprising thermodynamically stable clusters, initially 1 nm in size, cannot grow into sizes larger than 3 nm (more diameter) because the growth rate is slow (0.2 nm h^{-1}) relative to the coagulation sink[20] (2×10^{-3} s^{-1} for a 1-nm particle, decreasing to 2×10^{-4} s^{-1} for a 3-nm particle). At a vapour concentration of 14×10^6 cm^{-3} ($Q = 25 \times 10^3$ molecules cm^{-3} s^{-1}), the growth rate is significantly faster (1.1 nm h^{-1}). Therefore, it takes one-fifth of the time to reach sizes of 3 nm where particles can survive 10 times longer. Similarly, as the particle grows to 6 nm, its loss rate is reduced even further to 4×10^{-5} s^{-1}. In essence, this additional vapour source carries the nuclei over a coagulation loss barrier, resulting in a higher probability of the new particles surviving. If dimer nucleation of CIVs is considered[21], nucleation rates are predicted to increase to 10^2 cm^{-3} s^{-1} for a CIV concentration of 10^6 cm^{-3}, increasing further to 10^4 cm^{-3} s^{-1} for a CIV concentration of 10^7 cm^{-3}, so CIVs are likely to also contribute to the nucleation process.

Overcoming the coagulation loss barrier essentially increases the number and lifetime of condensation sites for production of cloud condensation nuclei (CCN) during the next days' cycle. Typically, the CCN concentration for clean marine air is 50–100 cm^{-3}, accounting for 10–20% of the aerosol population. The increase in the net input of particles into the aerosol population is likely to result in a similar percentage increase in available CCN (corresponding to ~10% of the new particles surviving to CCN sizes). Therefore, changes in the source rate of biogenic CIVs associated with global climate change are likely to significantly influence the CCN population. In fact, studies into the emissions of iodocarbons from marine biota have shown that emissions can increase by up to 5 times as a result of changes in environmental conditions associated with global change[14]. Therefore, increasing the source rate of CIVs fivefold will result in an increase in marine aerosol and CCN concentrations of the order of 20–60%. Changes in cloud albedo resulting from changes in CCN concentrations of this magnitude can lead to an increase in global radiative forcing similar in magnitude, but opposite in sign, to the forcing induced by greenhouse gases[22].

Although in some regions there is evidence for marine particle production from organic species[23], the proposed contribution of CIVs to the marine aerosol is most strongly supported by field measurements of marine aerosol composition[24–28]: iodine enrichment factors as high as 1,000 relative to bulk sea water have been found in marine aerosols globally, reaching factors as high as 33,000 in coastal zones. The present work confirms an aerosol nucleation mechanism involving CIVs in coastal regions, and suggests that CIVs enhance the production of particles in conjunction with dimethylsulphide-derived H_2SO_4 nucleation over remote oceans. CIVs could also contribute to the remote-ocean nucleation—but to confirm this, more theoretical and experimental advances into understanding the atmospheric iodine cycle need to be achieved. □

Methods

Laboratory experiments

Aerosol formation from the photolysis of CH_2I_2 in the presence of O_3 was investigated in the Caltech indoor chamber. This facility has been described previously[12], and consists of dual, 28-m^3 chambers illuminated by 300 1.22-m fluorescent lights which are used to simulate the ultraviolet and near-ultraviolet regions of ambient sunlight. The ultraviolet light intensity in the chamber was measured with a portable spectroradiometer (LI-1800, LI-COR, Lincoln), and was about 1.2 times the maximum intensity reaching the Earth's surface with a zenith angle of 0°, except for one low radiation experiment which was performed with one-quarter of the full intensity. The reaction chamber was filled with particle-free dry air at 20 °C that had been scrubbed of both volatile organic compounds and NO_x. CH_2I_2 (99% purity, Sigma-Aldrich) was dissolved in hexafluorobenzene (99% purity, Sigma-Aldrich), and the solution was evaporated into clean dry carrier air and injected into the chamber. After O_3 injection and allowing sufficient time for reactant mixing, the experiment was initiated by switching on the ultraviolet lights.

The evolution of the particle number concentration, number distribution, and hygroscopicity was monitored by condensation particle counters, differential mobility analysers, and a tandem differential mobility analyser, respectively, as described[12]. CH_2I_2 concentrations of 0.015 p.p.b. resulted in particle growth up to 30 nm (mode diameter), whereas for concentrations of 50 p.p.b., the maximum mode size reached was 200 nm. Particle composition was monitored using an Aerodyne aerosol mass spectrometer[29]. This spectrometer uses an aerodynamic lens inlet to focus the sampled particles into a narrow beam, which is then introduced into a high-vacuum chamber while the air is differentially pumped. The particles are vaporized on striking a heated, roughened molybdenum cartridge heater under high vacuum (10^{-7} torr) at about 600 °C. The vaporized species are then ionized by electron impact (70-eV electrons), and the positive ions produced are mass analysed with a quadrupole mass spectrometer. Particle aerodynamic diameter is determined by particle time-of-flight. The spectrometer can produce two types of data: mass spectra of the species present in/on the aerosol, and mass-weighed size distributions versus aerodynamic diameter at a series of m/z peaks of the mass spectrometer. The spectrometer used in these experiments was able to detect particles between about 40 nm and 1 μm, with a minimum detectable concentration of about 0.5 μg m^{-3}; it was calibrated for particle size with polystyrene latex spheres (Duke Scientific, Palo Alto).

Aerosol modelling

We used AEROFOR[7], a lagrangian-based 27-bin sectional box model which includes gas-phase chemistry and aerosol dynamics. The following processes are considered: (1) dimethylsulphide surface flux; (2) gas-phase oxidation of dimethylsulphide to SO_2/SO_3; (3) gas-phase oxidation of SO_2/SO_3 to H_2SO_4; (4) homogeneous nucleation of H_2SO_4, H_2O and NH_3; (5) condensation of CIVs, methane sulphonic acid, H_2SO_4 and H_2O onto pre-existing particles; (6) direct reaction of SO_2 with particles; (7) brownian coagulation of particles; (8) dry deposition to the sea surface. Full details can be found in ref. 7 and references therein. Cloud or precipitation processes are not included, and neither is heterogeneous removal of SO_2. The simulations are initialized with a typical marine aerosol concentration of 510 cm^{-3}, comprising an Aitken mode, accumulation mode, sea-salt jet drop mode and sea-salt film-drop mode, dimethylsulphide concentrations of 20 p.p.t., and NH_3 and SO_2 concentrations of 16 and 5 p.p.t., respectively. The air parcel undergoes adiabatic cycling in the boundary layer with relative humidity ranging from 70% at the surface to 99% at the top of the boundary layer.

Received 21 December 2001; accepted 16 April 2002; doi:10.1038/nature00775.

1. Slingo, A. Sensitivity of the Earth's radiation budget to changes in low clouds. *Nature* **343,** 49–51 (1990).
2. Charlson, R. J., Lovelock, J. E., Andreae, M. O. & Warren, S. G. Oceanic phytoplankton, atmospheric sulphur, cloud albedo and climate. *Nature* **326,** 655–661 (1987).
3. Katoshevski, D., Nenes, A. & Seinfeld, J. H. A study of processes that govern the maintenance of aerosols in the marine boundary layer. *J. Aerosol. Sci.* **30,** 503–532 (1999).
4. Capaldo, K. P., Kasibhatla, P. & Pandis, S. N. Is aerosol production within the remote marine boundary layer sufficient to maintain observed concentrations? *J. Geophys. Res.* **104,** 3483–3500 (1999).
5. Korhonen, P. *et al.* Ternary nucleation of H_2SO_4, NH_3, and H_2O in the atmosphere. *J. Geophys. Res.* **104,** 26349–26353 (1999).
6. Kulmala, M., Pirjola, L. & Mäkelä, J. M. Stable sulphate clusters as a source of new atmospheric particles. *Nature* **404,** 66–69 (2000).
7. Pirjola, L., O'Dowd, C. D., Brooks, I. M. & Kulmala, M. Can new particle formation occur in the clean marine boundary layer? *J. Geophys. Res.* **105,** 26531–26546 (2000).
8. O'Dowd, C. D. *et al.* A dedicated study of new particle formation and fate in the coastal environment (PARFORCE): Overview of objectives and achievements. *J. Geophys. Res.* (in the press).
9. Berresheim, H. *et al.* Gas-aerosol relationships of H_2SO_4, MSA and H: Observations in the coastal marine boundary layer at Mace Head, Ireland. *J. Geophys. Res.* (in the press).
10. Väkevä, M., Hämeri, K. & Aalto, P. Hygroscopic properties of nucleation mode and Aitken mode particles during and outside nucleation bursts in west coast of Ireland. *J. Geophys. Res.* (in the press).
11. Mäkelä, J. M. *et al.* Biogenic iodine emissions and identification of end-products in coastal ultrafine particles during nucleation bursts. *J. Geophys. Res.* (in the press).
12. Cocker, D. R., Flagan, R. C. & Seinfeld, J. H. State-of-the-art chamber facility for studying atmospheric aerosol chemistry. *Environ. Sci. Technol.* **35,** 2594–2601 (2001).
13. Carpenter, L. J. *et al.* Short-lived alkyl iodides and bromides at Mace Head, Ireland: Links to biogenic sources. *J. Geophys. Res.* **104,** 1679–1689 (1999).
14. Laturnus, F., Giese, B., Wiencke, C. & Adams, F. Low molecular-weight organoiodine and organobromine compounds released by polar macroalgae—the influence of abiotic factors. *Fresenius J. Anal. Chem.* **368,** 297–302 (2000).
15. Giese, B., Laturnus, F., Adams, F. C. & Wiencke, C. Release of volatile iodinated C_1-C_4 hydrocarbons by marine macro from various climate zones. *Environ. Sci. Technol.* **33,** 2432–2439 (1999).
16. Goodwin, K. D., North, W. J. & Lidstrom, M. E. Production of bromoform and dibromomethane by giant kelp: Factors affecting release and comparison to anthropogenic bromine sources. *Limnol. Oceaanogr.* **42,** 1725–1734 (1997).
17. Anache, S., Kamagata, Y., Kanagawa, T. & Kimuramatsu, Y. Bacteria mediate methylation of iodine in marine and terrestrial environments. *Appl. Environ. Microbiol.* **67,** 2718–2722 (2001).
18. McFiggans, G. *et al.* A model study of iodine chemistry in the marine boundary layer. *J. Geophys. Res.* **105,** 14371–14386 (2000).
19. Allan, B. J., Plane, J. M. C. & McFiggans, G. Observations of OIO in the remote marine boundary layer. *Geophys. Res. Lett.* **28,** 1945–1948 (2001).
20. Dal Maso, M., Kulmala, M., Mäkelä, J. M., Aalto, P. & O'Dowd, C. D. Condensation and coagulation sinks and the formation of nucleation mode particles in coastal and boreal forest boundary layers. *J. Geophys. Res.* (in the press).
21. Lushnikov, A. A. & Kulmala, M. Nucleation controlled formation and growth of disperse particles. *Phys. Rev. Lett.* **81,** 5165–5168 (1998).
22. Houghton, J. T. *et al. Climate Change 2001 – The Scientific Basis* (Cambridge Univ. Press, Cambridge, 2001).
23. Leck, C. & Bigg, E. K. Aerosol production over remote marine areas—A new route. *Geophys. Res. Lett.* **23,** 3577–3580 (1999).
24. Murphy, D. M., Thomson, D. S. & Middlebrook, A. M. Bromine, iodine and chlorine in single aerosol

particles at Cape Grim. *Geophys. Res. Lett.* **24,** 3197–3200 (1997).
25. Gäbler, H. E. & Heumann, K.-G. Determination of particulate iodine in aerosols from different regions by size fractioning impactor sampling and IDMS. *Int. J. Anal. Chem.* **50,** 129–146 (1993).
26. Wimschneider, A. & Heumann, G. Iodine: speciation in size fractioned atmospheric particles by isotope dilution mass spectrometry. *Fresenius J. Anal. Chem.* **353,** 191–196 (1995).
27. Baker, A. R., Thompson, D., Campos, M. L. A. M., Parry, S. J. & Jickells, T. D. Iodine concentration and availability in atmospheric aerosol. *Atmos. Environ.* **34,** 4331–4336 (2000).
28. Huang, S., Arimoto, R. & Rahn, K. A. Sources and source variations for aerosol at Mace Head, Ireland. *Atmos. Environ.* **35,** 1421–1437 (2001).
29. Jayne, J. T. *et al.* Development of an aerosol mass spectrometer for size and composition analysis of submicron particles. *Aerosol Sci. Technol.* **33,** 49–70 (2000).
30. Bloss, W. J., Rowley, D. M., Cox, R. A. & Jones, R. L. Kinetics and products of the IO self-reaction. *J. Phys. Chem. A* **105,** 7840–7854 (2001).

Acknowledgements

This work was funded by the European Commission, the Finnish Academy, the US Department of Energy and the National Development Plan and Environmental Protection Agency, Ireland.

Competing interests statement

The authors declare that they have no competing financial interests.

Correspondence and requests for materials should be addressed to C.D.O'D. (e-mail: colin.odowd@cmas.demon.co.uk).

Biodiversity as a barrier to ecological invasion

Theodore A. Kennedy*, Shahid Naeem†, Katherine M. Howe†, Johannes M. H. Knops‡, David Tilman* & Peter Reich§

* *Department of Ecology, Evolution, and Behavior, University of Minnesota, 1987 Upper Buford Circle, Saint Paul, Minnesota 55108, USA*
† *Department of Zoology, University of Washington, 24 Kincaid Hall, Box 351800, Seattle, Washington 98195-1800, USA*
‡ *School of Biological Sciences, University of Nebraska, 348 Manter Hall, Lincoln, Nebraska 68588-0118, USA*
§ *Department of Forest Resources, University of Minnesota, 1530 Cleveland Avenue North, Saint Paul, Minnesota 55108, USA*

Biological invasions are a pervasive and costly environmental problem[1,2] that has been the focus of intense management and research activities over the past half century. Yet accurate predictions of community susceptibility to invasion remain elusive. The diversity resistance hypothesis, which argues that diverse communities are highly competitive and readily resist invasion[3–5], is supported by both theory[6] and experimental studies[7–14] conducted at small spatial scales. However, there is also convincing evidence that the relationship between the diversity of native and invading species is positive when measured at regional scales[3,11,15,16]. Although this latter relationship may arise from extrinsic factors, such as resource heterogeneity, that covary with diversity of native and invading species at large scales, the mechanisms conferring greater invasion resistance to diverse communities at local scales remain unknown. Using neighbourhood analyses, a technique from plant competition studies[17–19], we show here that species diversity in small experimental grassland plots enhances invasion resistance by increasing crowding and species richness in localized plant neighbourhoods. Both the establishment (number of invaders) and success (proportion of invaders that are large) of invading plants are reduced. These results suggest that local biodiversity represents an important line of defence against the spread of invaders.

The relative contribution of extrinsic factors and resident diversity to invasion resistance varies across spatial scales[11,12]. For example, the initial arrival of propagules of invading plants into a formerly isolated region or field is regulated by extrinsic factors, such as human transport that breaches isolation. Similarly, if an invading plant lands on a bare patch within a field, extrinsic factors such as the frequency and intensity of disturbance, soil fertility and climate are likely to be more important than resident diversity in regulating the success of invaders. Within a field, however, in a vegetated patch, an invading plant will find itself surrounded by neighbouring plants, and it is here that biotic factors such as species composition and plant density will regulate the competitive environment the invader faces.

To test for the impacts of biodiversity on invasion resistance independent of extrinsic factors, we examined how variation in plant species richness among 147 experimental grassland plots at Cedar Creek, Minnesota, affected plant neighbourhood properties, and how these properties, in turn, affected the establishment and success of the 13 species of exotic non-native plants (primarily Eurasian, see Methods for species list) that invaded these plots. We focused on three properties of plant neighbourhoods that are widely used in studies of intra- and interspecific competition and have been shown to affect the performance of plants[17–19]. These properties are (1) the number of species within the neighbourhood (S_N), (2) the number of plants in the neighbourhood (N) and (3) θ_{sum} (ref. 12), an index of crowding that takes into account both the distance and size of all the plants within the neighbourhood.

Studies in which invading plants are established in neighbourhoods of a fixed size and composition[13,18] cannot test whether neighbourhood properties affect invasions in spatially heterogeneous systems like natural vegetation. We avoided this limitation by examining the neighbourhood properties of all naturally invading exotic plants, as well as the neighbourhood properties of 100 randomly placed 'null' positions, in each plot. The former neighbourhoods reflect the biotic environment where invaders successfully established, whereas the latter null neighbourhoods reflect the typical biotic environments found within the plot, independent of invader establishment.

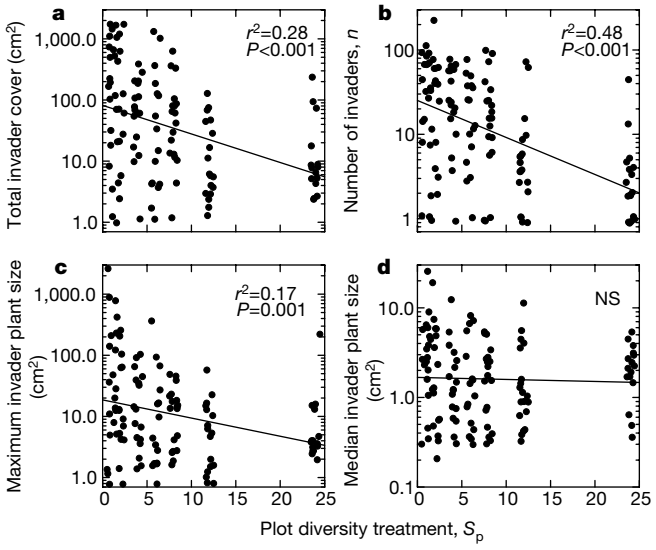

Figure 1 Plot diversity and invader performance. Effects of plot diversity treatment on total invader cover per subplot (**a**), the number of invading plants per subplot (**b**), the largest individual invader per subplot (**c**), and the median size of individual invaders in a subplot (**d**). Plot level patterns (**a**) are the result of a decrease in the number of invaders (**b**), and a reduction in the size of the largest invading plants in a subplot (**c**), but not a change in the median size of individual invaders (**d**), in more diverse plots. The least-squares regression lines are shown. Data are from 1998. Note the log scale on all *y* axes; NS, not significant.